Multiple Ca^{2+}-Binding Sites in the Extracellular Domain of the Ca^{2+}-Sensing Receptor Corresponding to Cooperative Ca^{2+} Response[†]

Yun Huang,[‡] Yubin Zhou,[‡] Adriana Castiblanco,[‡] Wei Yang,[‡] Edward M. Brown,[§] and Jenny J. Yang*,[‡]

Department of Chemistry, Center of Drug Design and Advanced Biotechnology, Georgia State University, Atlanta, Georgia 30303, and Division of Endocrinology, Diabetes and Hypertension, Department of Medicine, Brigham and Women's Hospital and Harvard Medical School, Boston, Massachusetts 02115

Received August 3, 2008; Revised Manuscript Received October 29, 2008

ABSTRACT: A small change in the extracellular Ca^{2+} concentration ($[Ca^{2+}]_o$) integrates cell signaling responses in multiple cellular and tissue networks and functions via activation of Ca^{2+}-sensing receptors (CaSR). Mainly through binding of Ca^{2+} to the large extracellular domain (ECD) of the dimeric CaSR, intracellular Ca^{2+} responses are highly cooperative with an apparent Hill coefficient ranging from 2 to 4. We have previously reported the identification of two continuous putative Ca^{2+}-binding sites by grafting CaSR-derived, Ca^{2+}-binding peptides to a scaffold protein, CD2, that does not bind Ca^{2+}. In this paper, we predict more potential noncontinuous Ca^{2+}-binding sites in the ECD. We dissect the intact CaSR into three globular subdomains, each of which contains two to three predicted Ca^{2+}-binding sites. This approach enables us to further understand the mechanisms underlying the binding of multiple metal ions to extended polypeptides derived from a location within the ECD of the CaSR, which would be anticipated to more closely mimic the structure of the native CaSR ECD. Tb^{3+} luminescence energy transfer, ANS fluorescence, and NMR studies show biphasic metal-binding components and Ca^{2+}-dependent conformational changes in these subdomains. Removing the predicted Ca^{2+}-binding ligands in site 1 and site 3 abolishes the first binding step and second binding step, respectively. Studies on these subdomains suggest the existence of multiple metal-binding sites and metal-induced conformational changes that might be responsible for the switching on and off the CaSR by the transition between its open inactive form and closed active form.

The Ca^{2+}-sensing receptor (CaSR) is a seven-transmembrane protein that belongs to family C of the superfamily of G protein-coupled receptors (GPCRs), which also includes metabotropic glutamate receptors (mGluR1−8), heterodimeric γ-aminobutyric acid B (GABAB) receptors, taste (T1R) receptors, the promiscuous L-α-amino acid receptor (GPRC6A), and several orphan receptors (*1*). Most of these receptors are characterized by a large extracellular domain (ECD) at the N-terminus, which binds various endogenous agonists. Many physiological functions regulated by the family C GPCRs are mediated through agonist-mediated allosteric modulation of the respective ECDs; thus, understanding the properties of ligand-binding sites is crucial for drug design. The CaSR was first cloned by Brown et al. from bovine parathyroid gland more than a decade ago (*2*). After removal of the N-terminal, 20-residue signal peptide, the functional form of the CaSR contains an ECD with more than 600 residues and shares 27% sequence identity with the corresponding segment of the mGluRs (*3*).

The CaSR responds to small changes in $[Ca^{2+}]_o$ by modulating multiple signaling pathways, including activation of phospholipases C, A_2, and D, and inhibition of cAMP production (*4, 5*). It is thought that binding of Ca^{2+} to multiple binding sites within the large extracellular domain (ECD) of the CaSR produces intracellular Ca^{2+} responses ($[Ca^{2+}]_i$) that are highly cooperative, with an apparent Hill coefficient ranging from 2 to 4 (*6*). More than 200 mutations and polymorphisms have been identified in the CaSR that either inactivate (e.g., have a reduced response to $[Ca^{2+}]_o$) or activate (have an enhanced response to $[Ca^{2+}]_o$) the receptor and are associated with a number of human diseases, including familial hypocalciuric hypercalcemia (FHH), neonatal severe hyperparathyroidism (NSHPT), and autosomal dominant hypoparathyroidism (ADH) (*7−10*), which can change the Ca^{2+} response of the CaSR with regard to its cooperativity and selectivity.

The ECD regions have been proposed to contain the major Ca^{2+}-binding sites and to respond to extracellular Ca^{2+} ($[Ca^{2+}]_o$) for both the mGluRs and the CaSR, although various regions in the transmembrane segments have also been shown to bind Ca^{2+} (*6, 11, 12*). While X-ray crystallography has been the main tool for studying the structure of metal-binding sites (*13−15*), no bound Ca^{2+} has been observed in the structures of mGluR1 determined with or without its ligand, glutamate (*16*). To date, successful crystallization of the CaSR ECD has not been reported despite a decade or more of efforts directed to this end.

[†] This work was supported, in part, by National Institutes of Health Grants GM62999-1 and GM081749-01, National Science Foundation Grant MCB-0092486, American Heart Association Grant 0655168B (to J.J.Y.), and a Predoctoral Fellowship from the Brain and Behavior Program at Georgia State University (to Y.H.).

* To whom correspondence should be addressed. E-mail: chejjy@langate.gsu.edu.

[‡] Georgia State University.

[§] Brigham and Women's Hospital and Harvard Medical School.

10.1021/bi8014604 CCC: \$40.75

Progress in understanding the mechanism underlying CaSR-mediated responses to extracellular Ca^{2+} signals has largely been hampered by a lack of knowledge regarding the Ca^{2+}-binding sites in this protein (*4*). While measurement of high $[Ca^{2+}]_o$-evoked increases in $[Ca^{2+}]_i$ (with a Hill coefficient of 2−4) suggests that the CaSR has multiple Ca^{2+}-binding sites, it is not clear how this extracellular Ca^{2+}-sensing protein manages to cooperatively respond to small changes in $[Ca^{2+}]_o$ within a narrow physiological window (1.1−1.3 mM).

With GG (*17*) and MetalFinder (*18, 19*), a computational algorithm developed in our laboratory based on geometric description, graph theory, and key structural features associated with Ca^{2+}-binding sites in proteins, we have identified at least five putative Ca^{2+}-binding sites in the CaSR on the basis of model structures (*17*). Two continuous putative Ca^{2+}-binding sites (denoted site 3 and site 5 in this work) were reported to exhibit intrinsic Ca^{2+} binding capability that could be probed upon grafting of the respective peptides containing these sites into a scaffold, non-Ca^{2+}-binding protein, CD2[1] (*19*). However, it is not clear whether these putative Ca^{2+}-binding sites are able to bind Ca^{2+} in an environment more closely resembling that of the native protein. The cooperative Ca^{2+} binding properties of these predicted Ca^{2+}-binding sites were also not examined. In this paper, we applied a subdomain approach to further understand the mechanisms of multiple metal-binding processes by dissecting the intact CaSR ECD into three globular subdomains, each of which contains two to three predicted Ca^{2+}-binding sites. Studies of these subdomains suggested the existence of multiple metal-binding processes and metal-induced conformational changes that might be responsible for switching on and off the CaSR by promoting transitions between its opened inactive form and closed active form.

MATERIALS AND METHODS

Computational Prediction of Ca^{2+}-Binding Sites from a Model Structure. The sequences of the ECD regions (residues 1−540) of the human CaSR and mouse mGluR were aligned with CLUSTALW (*20*), and the structural modeling of the CaSR was performed using SWISS-MODEL (*21, 22*) and the MODELER (*23*) based on the structure of mGluR1 [PDB entries 1EWT (*16*) and 1ISR (*24*)]. As described previously, the putative Ca^{2+}-binding sites in the CaSR were predicted using MetalFinder (*18, 19*), and the electrostatic potentials were calculated using DelPhi (*25, 26*).

Protein Engineering, Expression, and Purification. Three subdomains were amplified from CaSR-pCDNA 3.1(+) (*27*) and were further subcloned into the pRSET-A vector between the *Bam*HI and *Eco*RI restriction sites. Site-directed mutagenesis was carried out as described previously (*19*). As shown in Figure 1, subdomain 1 (amino acids 132−300) contains three predicted Ca^{2+}-binding sites (sites 1−3), subdomain 2 (amino acids 185−324) has two predicted Ca^{2+}-binding sites (sites 2 and 3), and subdomain 3 (amino acids 340−445) includes two putative Ca^{2+}-binding sites (sites 4 and 5). All the DNA sequences were verified by automated sequencing on an ABI PRISM-377 DNA sequencer (Applied Biosystems).

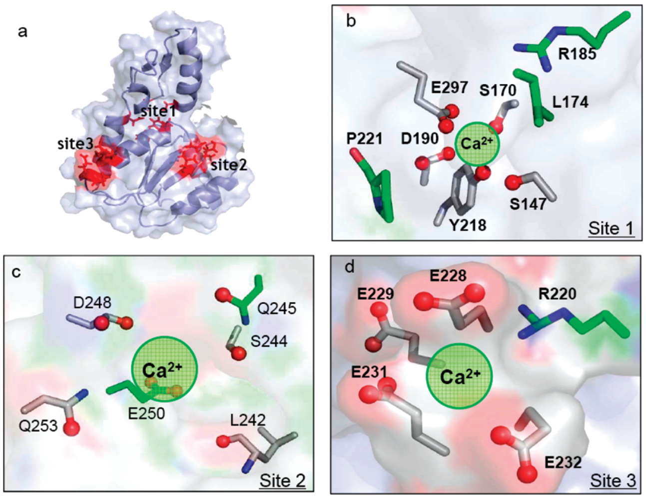

FIGURE 1: Location of predicted Ca^{2+}-binding sites and some disease-associated mutations in the CaSR. (a) Modeled structure of subdomain 1 (S132−A300), which contains three putative Ca^{2+}-binding sites (sites 1−3). (b) Predicted site 1 is located in the hinge region of the ECD of the CaSR. (c and d) Predicted sites 2 and site 3. Ca^{2+}-binding ligand residues are colored gray, whereas the disease-associated residues are colored green.

The recombinant proteins were expressed as His_6-tag fusion proteins in *Escherichia coli* BL21(DE3)pLysS, Rosetta(DE3), or Tuner(DE3)pLacI cells transformed with the plasmid constructs in LB medium with 100 mg/L ampicillin, and the cells were grown at 37 °C. Isopropyl *β*-D-thiogalactopyranoside (IPTG) (100−400 *μ*M) was added when the OD_{600} reached 0.6 to induce protein expression for an additional 3−4 h, and cell pellets were collected by centrifugation and stored at −20 °C. The cell pellets were subsequently resuspended in lysis buffer [1% sarcosine and 1 mM EDTA in PBS (pH 7.4)] and subjected to sonication. After centrifugation, the clarified supernatants were subjected to affinity chromatography using the Hitrap Ni^{2+}-chelating column (GE Healthcare). The eluates containing the target proteins were extensively dialyzed against 10 mM Tris-HCl buffer (pH 7.4) to remove the residual imidazole. The concentrations of proteins and their mutants were determined using absorption at 280 nm with extinction coefficients of 36130 M^{-1} cm^{-1} for subdomain 1, 34850 M^{-1} cm^{-1} for subdomain 2, and 27550 M^{-1} cm^{-1} for subdomain 3. All the extinction coefficients were calculated from primary sequences according to the method by Gill and von Hippel (*28*).

Circular Dichroism Spectroscopy. The CD spectra of samples were recorded in a Jasco-810 spectropolarimeter at 25 °C. For far-UV CD measurements, the protein concentrations ranged from 15 to 20 *μ*M, and spectra were recorded using a 1 mm path length cell. For near-UV CD, the protein samples at 100 *μ*M were used with a 1 cm path length cell. All spectra were obtained as the average of at least 10 scans with a scan rate of 50 nm/min. The ellipticity was measured from 190 to 260 nm or from 250 to 320 nm and then converted to mean residue molar ellipticity after subtracting the spectrum of the buffer as the blank.

Fluorescence Spectroscopy. Fluorescence emission spectra were recorded on a PTI fluorimeter at 25 °C using a 1 cm path length cell. Intrinsic tryptophan fluorescence spectra

---

[1] Abbreviations: CD2, cluster of differentiation 2; EGTA, ethylene glycol tetraacetic acid; PBS, phosphate-buffered saline; NMR, nuclear magnetic resonance; PTH, parathyroid hormone.

were recorded from 300 to 400 nm with the excitation wavelength at 282 nm. The slit widths were set as 2 and 4 nm for excitation and emission, respectively. For Tyr/Trp-sensitized Tb^{3+} luminescence energy transfer (Tb^{3+}-LRET) experiments, emission spectra were collected from 500 to 600 nm with the excitation at 282 nm. Slit widths for excitation and emission were set at 8 and 12 nm, respectively. Protein samples with concentrations ranging from 2 to 3 μM were prepared in 20 mM PIPES, 120 mM NaCl, and 10 mM KCl (pH 6.8) to prevent Tb^{3+} precipitation. A glass filter with a cutoff of 320 nm was used to circumvent secondary Raleigh scattering. Protein samples were titrated with Tb^{3+} by gradually adding appropriate volumes of Tb^{3+} stock solutions. Two Tb^{3+} stocks, 100 μM and 1 mM, were prepared for the titration experiment. Both stocks contained the same concentrations of proteins being studied in the respective experimental protocols to prevent dilution of the protein during addition of the Tb^{3+}. For the first binding process, 5−10 μL aliquots of the 100 μM Tb^{3+} stock were added to a 1 mL solution until the first binding process reached a plateau (10−15 points). Aliquots (5 μL) of a 1 mM Tb^{3+} stock were subsequently added to achieve saturation of the second binding process (8−12 points). The total stock volume used was around 200−250 μL. Fifteen minutes was allowed for equilibration of metal binding following each addition of Tb^{3+} prior to the next addition. For each data point, the contribution of the Tb^{3+} background signal was subtracted using the fluorescence of the respective Tb^{3+} solutions without protein as a control. The fluorescence intensity was normalized by subtracting the contribution of the baseline slope using logarithmic fitting. All the experiments were repeated at least three times. For biphasic binding processes, the first step of Tb^{3+} binding to the protein was obtained by fitting normalized fluorescence intensity data using the equation

$$f = \left[([P]_T + [M]_T + K_d) - \sqrt{([P]_T + [M]_T + K_d)^2 - 4[P]_T[M]_T}\right] / 2[P]_T \tag{1}$$

where f is the fractional change, K_d is the dissociation constant for Tb^{3+}, and $[P]_T$ and $[M]_T$ are the total concentrations of protein and Tb^{3+}, respectively.

The second cooperative metal binding step is fitted using the equation

$$\Delta S = \Delta S_1 + \Delta S_2 \frac{[M]^n}{K_d^{\,n} + [M]^n} \tag{2}$$

where ΔS_1 and ΔS_2 are the corresponding signal changes for each process, K_d is the apparent binding affinity, and n is the Hill coefficient for the second binding component, whereas [M] is the free metal concentration and ΔS the total signal change in the equation.

For metal-binding to subdomain 3, the binding affinity was fitted by the Hill equation

$$\Delta S = \frac{[M]^n}{K_d^{\,n} + [M]^n} \tag{3}$$

where ΔS is the total signal change in the equation, K_d is the apparent binding affinity, n is the Hill coefficient, and [M] is the free metal concentration.

ANS Binding Measurement. For the ANS (8-anilino-1-naphthalenesulfonic acid) binding assay, protein samples were incubated with 40 μM ANS in 50 mM Tris-HCl and 100 mM KCl (pH 7.4) with either 5 mM EGTA or 5 mM Ca^{2+} at room temperature for 1 h prior to measurement. The excitation wavelength was set at 370 nm, and the emission spectra were acquired from 400 to 600 nm. For the Ca^{2+} titration, the protein concentration was 3 μM and the Ca^{2+} concentration was varied from 0 to 30 mM in 20 mM Tris-HCl and 50 mM KCl (pH 7.4). The free Ca^{2+} concentration in the buffers used in this study without Chelex-100 treatment has been measured to be <10 μM using BAPTA, a calcium-specific chelator (data not shown). In view of this, we have paid careful attention to potential contamination by background Ca^{2+} in buffers and proteins during our initial pilot titration experiments. All buffers were pretreated with Chelex-100 (Bio-Rad). All the glassware and plasticware used in the preparation of samples were pretreated with 2% HNO_3 (optima grade; Fisher Scientific) and then rinsed with Chelexed, double-distilled water. Protein samples were extensively dialyzed against Chelex-100-treated buffers. Under such stringent conditions, the Ca^{2+} dissociation constant was determined to be ~0.7 mM for the "high-affinity" Ca^{2+}-binding site, a value which is at least >70-fold higher than the free, background Ca^{2+} concentration in the buffers even without Chelex-100 treatment. Given this fact, we carried out subsequent titration experiments using buffers that were not pretreated with Chelex-100.

Analysis of the Gibbs Free Energy of Metal Binding to Subdomains. The Gibbs free energies of metal binding to subdomains (the second transition for subdomain 1 and subdomain 2, as well as subdomain 3) were obtained by fitting the Ca^{2+} or Tb^{3+} titration data to the model-independent two-site Adair function as previously described (*29, 30*):

$$f = \frac{e^{-\Delta G_1/RT}[M] + 2e^{-\Delta G_2/RT}[M]^2}{2(1 + e^{-\Delta G_1/RT}[M] + e^{-\Delta G_2/RT}[M]^2)} \tag{4}$$

M stands for metal ions. The sum of the two intrinsic free energies of a subdomain ($\Delta G_I + \Delta G_{II}$) is given by the macroscopic free energy ΔG_1, and the total free energy of metal binding ($\Delta G_I \Delta G_{II} \Delta G_{I-II}$) to both sites in each subdomain is given by the term ΔG_2. The term ΔG_{I-II} accounts for any positive or negative intradomain cooperativity within subdomains. It is not possible to obtain intradomain cooperative energy merely from the fluorescence titration data; however, the lower limit of the cooperative free energy (ΔG_c) can be estimated by assuming that both sites in each subdomain have equal intrinsic binding constants ($\Delta G_I = \Delta G_{II}$), which is defined as

$$\Delta G_c = \Delta G_2 - 2\Delta G_1 - RT \ln 4 \tag{5}$$

Fluorescence Quenching by Acrylamide. Acrylamide quenching was performed to assess the solvent accessibility of Trp residues in subdomains before and after the addition of Ca^{2+}. A 1 mL solution of 5 μM protein in 50 mM Tris, 135 mM NaCl, and 10 mM KCl (pH 7.4) was titrated with 10−20 μL aliquots of a 4 M acrylamide stock solution in the same buffer. All quenching experiments were conducted at 22 °C and repeated three times. The samples were excited at 295 nm, and the fluorescence spectra were recorded from 310 to 450 nm. The integrated fluorescence intensity from

Table 1: Properties of Subdomains and Predicted Ca^{2+}-Binding Sites in Each Subdomain

protein	amino acid from CaSR	location	Cys no.	PI	molecular mass (kDa)	predicted Ca^{2+}-binding sites	mutations
subdomain 1	S132−A300	lobe 1 lobe 2	1	4.95	22.9	site 1 (S147, S170, D190, Y218, E297) site 2 (D215, L242, S244, D248, Q253) site 3 (E224, E228, E229, E231, E232)	mutation 1 (D190A/E297I) mutation 2 (D215A/D248A) mutation 3 (E224I/E228I/E229I/E231I/E232I)
subdomain 2	R185−A324	lobe 2	1	4.62	20.3	site 2 (D215, L242, S244, D248, Q253) site 3 (E224, E228, E229, E231, E232)	
subdomain 3	A323−G494	lobe 1	5	5.05	23.8	site 4 (E350, E353, E354, N386, S388) site 5 (E378, E379, T396, D398, E399)	mutation 4 (E350I/E353I/E354I) mutation 5 (E378I/E379I/D398A/E399I)

310 to 450 nm was plotted as a function of the acrylamide concentration and analyzed according to a modified Stern−Volmer equation by taking into account both collisional and static quenching:

$$\frac{F_0}{F} = (1 + K_{SV}[Q])e^{V[Q]} \qquad (6)$$

where F_0 and F are the tryptophan fluorescence intensities in the absence and presence of the quencher, respectively, K_{SV} is the collisional quenching constant, V is the static quenching constant, and [Q] is the quencher concentration.

NMR Spectroscopy. One-dimensional ^1H spectra were recorded at 25 °C on a Varian 500 MHz NMR spectrometer with a spectral width of 6600 Hz. Protein samples (~300 μM) were used in 20 mM PIPES, 150 mM KCl, and 10% D_2O (pH 6.8). Appropriate amounts of Ca^{2+} stock solutions were gradually added into the NMR sample tube. FELIX98 (MSI) was used to process NMR data with an exponential line broadening window function of 2 Hz and the suppression of water signal with a Gaussian deconvolution function having a width of 20.

Measurement of $[Ca^{2+}]_i$ in Cell Populations by Fluorimetry. The $[Ca^{2+}]_i$ responses of wild-type and mutant CaSRs were assessed as described by Bai et al. (*27*). In brief, HEK293 cells transfected with the CaSR or its mutant cDNAs were loaded with Fura-2AM, and the remaining extracellular Fura-2AM was washed out before the cells were transferred into a fluorescence cuvette. The fluorescent emission at 510 nm was collected with excitation at 340 and 380 nm at varying $[Ca^{2+}]_o$ values (0.5−20.5 mM). The ratio of the fluorescence intensities is used to derive the level of $[Ca^{2+}]_i$.

RESULTS

Design of Subdomains of CaSR. Three-dimensional, globular lobes 1 and 2 are formed by discontinuous protein sequences in the ECD. Figure 1 and Table 1 show the design and model structures of the subdomains based on homology modeling of the different forms of mGluR1 (*19*). Using our previously developed computational algorithms (*17*), we have predicted several potential Ca^{2+}-binding pockets in the CaSR (*19*). These predicted Ca^{2+}-binding sites could be organized into two classes as shown in Figure 1 and Table 1, two continuous Ca^{2+}-binding sites (sites 3 and 5), and three noncontinuous Ca^{2+}-binding sites (sites 1, 2, and 4).

The predicted site 1, formed by S147, S170, D190, Y218, and E297, is located within the hinge region of the ECD. Residues of predicted site 2 (D215, L242, S244, D248, and Q253) and site 3 (E224, E228, E229, E231, and E232) are in the first half of the sequence of lobe 2 (amino acids 215−253), whereas predicted Ca^{2+}-binding sites 4 (E350, E353, E354, N386, and S388) and 5 (E378, E379, T396, D398, and E399) are clustered in the second half of lobe 1 (amino acids 350−400).

Our design of three subdomains of the CaSR is based on four criteria. First, a well-folded globular protein domain is preferred to ensure the formation of an intact Ca^{2+}-binding site. To avoid disruption of structural integrity, the domain boundary is chosen near an unstructured or loop region according to our modeled structure and secondary structure prediction using PHD (*31*) and PSIPRED (*32*). Second, a size of <30 kDa is preferred since such a size will allow us to use high-resolution NMR to monitor the Ca^{2+} binding event. Third, the cysteine-rich region within the C-terminal portion of the ECD is not included, since it has been shown to play less important roles in the Ca^{2+} responsiveness of the CaSR (*33*). In addition, the cysteine residues, Cys129 and Cys131, which participate in intermolecular disulfide bonds between the CaSR monomers in the biologically active CaSR dimer are excluded to limit cooperative effects to those occurring within monomeric subdomains and since they are less likely to be important for the Ca^{2+} response (e.g., increase in $[Ca^{2+}]_i$) (*34*). To obtain the Ca^{2+} binding affinity of site 1 and to estimate cooperativity, it is important to have a sequence that encompasses site 1 since this site has been shown to be highly important for the proper Ca^{2+} response (*35*). According to these criteria, subdomain 1, which spans both lobes 1 and 2, ranges from S132 to A300 and contains putative Ca^{2+}-binding sites 1−3; subdomain 2 (amino acids R185−A324) contains sites 2 and 3 in lobe 2, and subdomain 3 (amino acids A323−G494) contains sites 4 and 5 (Figure 1, Table 1, and Figure S1a,b of the Supporting Information). All these proteins were successfully purified to near homogeneity with more than 90% purity (Figure S1c of the Supporting Information).

Designed Subdomains Are Folded and Bind Ca^{2+}. To ensure that the designed subdomains have proper structures, we carried out conformational analysis using various biophysical methods. First, we examined the secondary and tertiary structures of the subdomains using CD spectroscopy. As shown in Figure 2a, the far-UV CD spectra of subdomains 1−3 exhibited negative maxima at 208 and 222 nm, suggesting the existence of substantial helical structure as predicted in the model structure. Next, we examined the intrinsic fluorescence of the subdomains, since each of them contains two or three tryptophans. Upon excitation at 282 nm, the Trp fluorescence spectra of subdomains 1−3

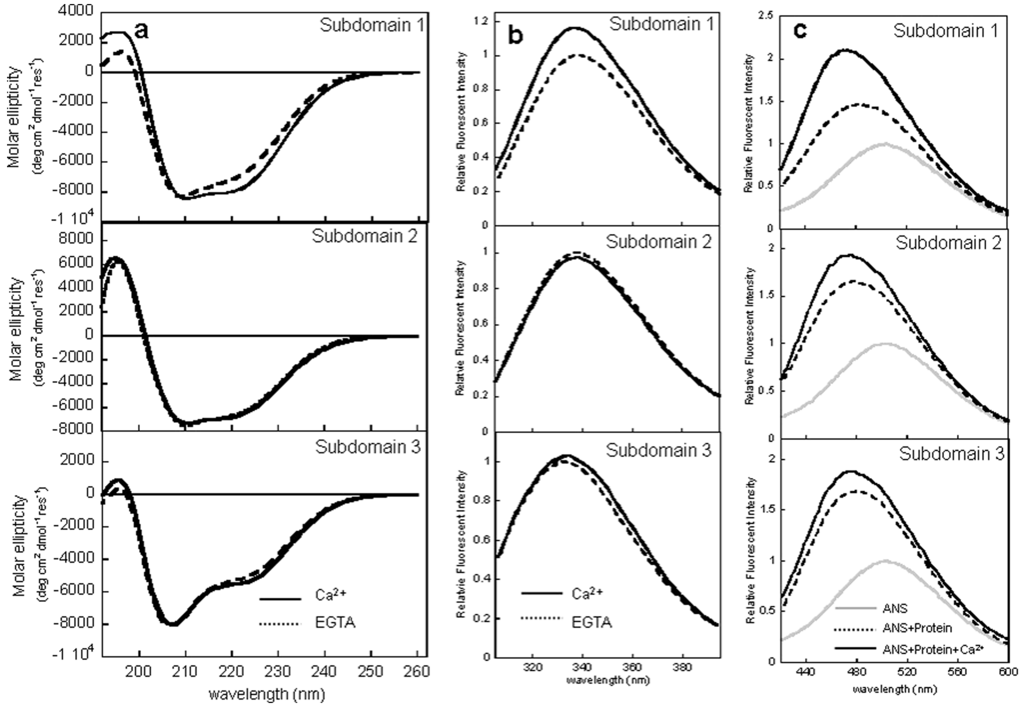

FIGURE 2: CD and fluorescence spectra of subdomains in the absence (– – –) or presence (—) of 5 mM Ca^{2+}. The top, middle, and bottom panels for each diagram represent spectra from subdomains 1−3, respectively: (a) far-UV CD spectra and (b) Trp fluorescence spectra of subdomains with 5 mM EGTA or 5 mM Ca^{2+}. (c) ANS fluorescence spectra of ANS alone (gray line) and ANS complexed with subdomains with 5 mM EGTA (---) or 5 mM Ca^{2+} (—).

exhibited emission maxima at 339, 338, and 334 nm, respectively (Figure 2b). Moreover, the near-UV CD spectra of subdomain 1 showed significant bands in regions corresponding to immobilized aromatic residues (280−300 nm) (Figure S2a of the Supporting Information). In subdomain 1, the peaks at 262 and 268 nm arise from the L_b transition of phenylalanine and the peaks around 288 and 297 nm are attributed to the L_b transition of tryptophan. The positive band in the range of 274−280 nm comes from the L_a transition of tryptophan. To further estimate the overall solvent accessibility of the tryptophan residues within each subdomain, we performed additional fluorescence quenching studies with acrylamide. As shown in Figure S2b of the Supporting Information, the fully exposed free L-tryptophan has a K_{sv} of 20.9 M^{-1}, whereas the apparent collisional quenching constants (K_{sv}) for subdomains 1−3 are 3.7, 13.4, and 3.8 M^{-1}, respectively. All these results suggest that the aromatic residues in these three subdomains were at least partially buried, as in other folded proteins.

Ca^{2+}-Induced Conformational Changes in Subdomains. As shown in Figure 2a−c (solid lines), the addition of saturating amounts of Ca^{2+} results in changes in both the Trp fluorescence and CD spectra of the respective subdomains. Notably, more negative signals were acquired above 210 nm for subdomains 1 and 3, suggesting the formation of greater helical contents or the rearrangement of secondary structure induced by Ca^{2+} in these two proteins. In addition, Ca^{2+} induced tertiary structural changes in subdomain 1, as suggested by substantially more prominent near-UV CD bands around 275 and/or 288 nm (Figure S2a of the Supporting Information). Ca^{2+}-induced CD signal changes were not significant in subdomain 2. Furthermore, binding of Ca^{2+} leads to a 3 nm blue shift of the emission maxima, a 15% increase in Trp fluorescence intensity in subdomain 1, and slight intensity changes in both subdomains 2 and 3 (Figure 2b). Consistent with the changes in fluorescence intensity, the acrylamide quenching studies revealed that the apparent collisional quenching constants for the subdomains were decreased by 10−18% (Figure S2b and Table S1 of the Supporting Information). ANS, a widely used hydrophobic probe, was also used to characterize Ca^{2+}-induced conformational changes. Compared to those of the Ca^{2+}-depleted proteins, the ANS fluorescence spectra of subdomain 1 in the presence of Ca^{2+} underwent a 12 nm blue shift and further exhibited a 30% increase in fluorescence intensity (Figure 2c), suggesting Ca^{2+}-induced exposure of more hydrophobic regions in this protein. Similar intensity increases, though to lesser extents, were detected in subdomains 2 (15%) and 3 (10%), suggesting that Ca^{2+} induced conformational changes in all three subdomains.

More importantly, such Ca^{2+}-induced blue shifts of emission maxima, as well as the enhancement in the Trp fluorescence (Figure 3a) or ANS fluorescence intensities (Figure 3b), were significantly decreased or abolished after mutation of predicted Ca^{2+}-binding ligand residues in subdomain 1 [i.e., E297I/D190A in site 1 (subdomain 1, mutation 1), D215A/D248A in site 2 (subdomain 1, mutation 2), or E224I/E228I/E229I/E231I/E232I in site 3 (subdomain 1, mutation 3)]. Similar phenomena were observed within subdomain 3 and its mutants (data not shown). Thus, the Ca^{2+}-induced conformational changes primarily arose from its binding to the predicted sites but were not due to its nonspecific binding to other negatively charged regions.

Multiple Metal Binding Processes. According to the model structure of the ECD of the CaSR, the Trp residues in the subdomains are within 5−10 Å of the closest predicted metal-binding pocket, thus making it possible to use aromatic residue-sensitized Tb^{3+} luminescence resonance energy transfer (Tb^{3+}-LRET) to monitor the binding process. As a trivalent Ca^{2+} analogue, Tb^{3+} has been widely used to probe

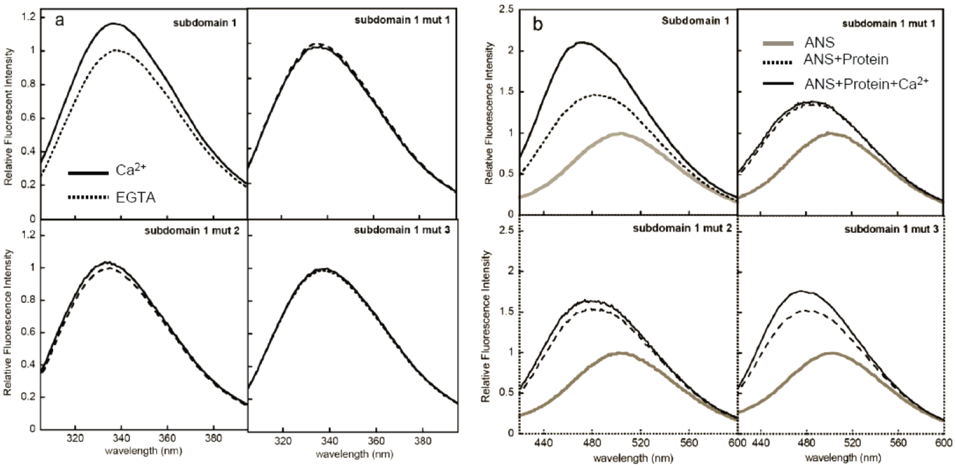

FIGURE 3: Ca^{2+}-induced changes in Trp and ANS fluorescence in subdomains and their charged ligand mutants [subdomain 1, mutation 1 (E297I/D190A); subdomain 1, mutation 2 (D215A/D248A); and subdomain 1, mutation 3 (E224I/E228I/E229I/E231I/E232I)]. (a) Trp fluorescence spectra of subdomain 1 and its mutants in the presence of 0 (---) and 5 mM Ca^{2+} (—). (b) ANS fluorescence spectra of subdomain 1 and its mutants in the presence of 0 (---) and 5 mM Ca^{2+} (—). The spectrum of ANS alone is shown as a gray line.

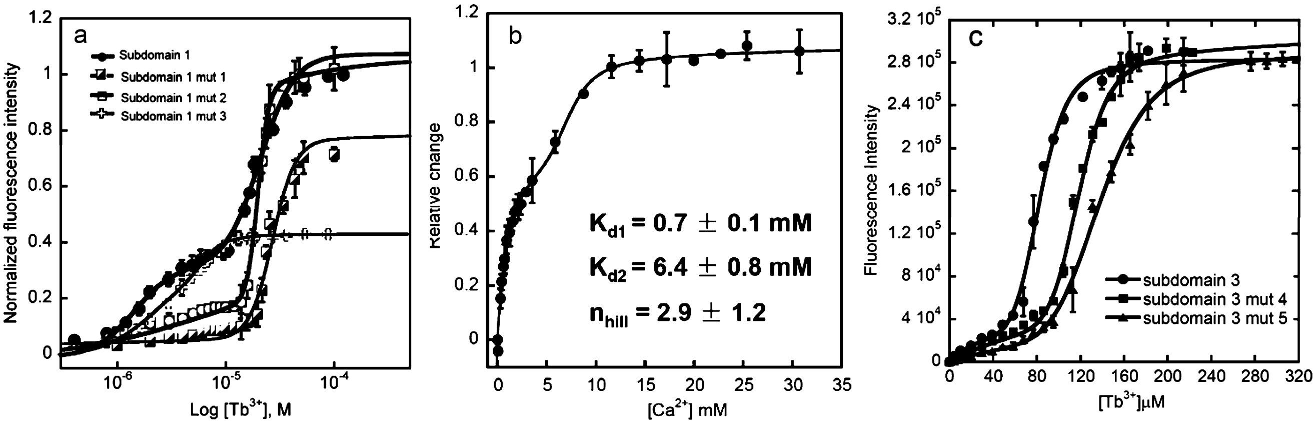

FIGURE 4: Metal titration of subdomains and their mutants. (a) Tb^{3+} titration curve of subdomain 1 and its mutants. (b) Ca^{2+} titration curve of subdomain 1. ANS fluorescence changes were monitored during Ca^{2+} titration. (c) Tb^{3+} titration curve of subdomain 3 and its mutants. The buffer for Tb^{3+} titration consisted of 20 mM PIPES, 135 mM NaCl, and 10 mM KCl (pH 6.8). The buffer for Ca^{2+} titration contained 50 mM Tris-HCl and 50 mM KCl (pH 7.4). The titration curve is fitted as described in Materials and Methods.

Table 2: Tb^{3+} Dissociation Constants for Subdomains and Their Mutants

protein	K_{d1} for transition 1 (μM)	K_{d2} for transition 2 (μM)
subdomain 1	0.8 ± 0.3	13.2 ± 0.9
subdomain 1, mutation 1	not available	28.4 ± 0.5[a]
subdomain 1, mutation 2	2.2 ± 0.5	21.5 ± 2.7[b]
subdomain 1, mutation 3	10.8 ± 4.3[b]	not available
subdomain 2	18.0 ± 5.8[b]	27.7 ± 2.6[a]

protein	K_d (μM)	n_{hill}
subdomain 3	82.0 ± 1.2	5.8 ± 1.2
subdomain 3, mutation 4	117.1 ± 2.7[a]	5.5 ± 1.9
subdomain 3, mutation 5	132.6 ± 7.9[b]	5.1 ± 1.3

[a] $P < 0.01$. [b] $P < 0.05$.

Ca^{2+}-binding sites due to their similarities in ionic radii and coordination chemistry. The advantages of using Tb^{3+} are threefold. First, its spectroscopic properties for energy transfer between aromatic residues close to the binding pocket and Tb^{3+} bound in the pocket not only give quantitative measurements of K_d but also help to reveal structural information. Second, its +3 charge, combined with an affinity higher than that of Ca^{2+}, is a big plus in studying metal binding properties of proteins with weak K_d values. Third, the level of background contamination of Tb^{3+} is lower than that of Ca^{2+}. A notable biphasic Tb^{3+} binding process was observed in subdomain 1, which contains three predicted Ca^{2+}-binding sites (sites 1−3), as shown in Figure 4a. The first step could be fitted by a 1:1 binding process with a dissociation constant (K_d) of 0.8 ± 0.3 μM. The second step can be fitted by a cooperative Hill equation with an apparent K_d of 13.2 ± 0.9 μM and a Hill coefficient of 2.3 ± 0.1 (Table 2). For subdomain 3, a cooperative Tb^{3+} binding curve was obtained with a dissociation constant of 82.0 ± 1.2 μM and a Hill coefficient of 6 (Figure 4c and Table 2).

We generated a series of charged ligand mutations at each predicted site to knock out metal binding capability and compare resultant changes in metal binding behavior. As one can see in Figure 4a and Table 2, mutations of predicted site 1 (subdomain 1, mutation 1) resulted in almost complete loss of the first component of the titration curve with a K_d of 28.4 ± 0.5 μM for the second step, whereas mutations of predicted site 3 (subdomain 1, mutation 3) led to the elimination of the second phase of the titration curve and exhibited a K_d of 10.8 ± 4.3 μM for the first step. In the site 2 mutant of subdomain 1 (subdomain 1, mutation 2), the biphasic binding curve still exists. However, mutations resulted in a >50% decrease in the fluorescence enhancement

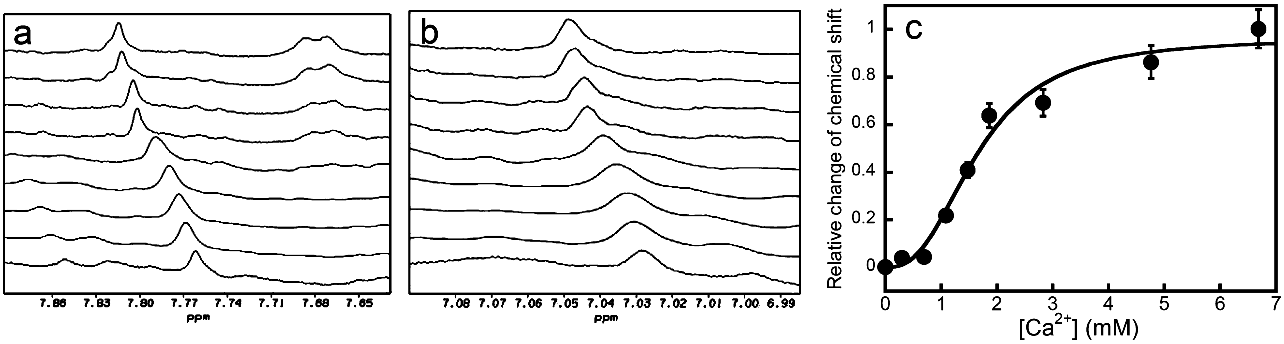

FIGURE 5: Ca^{2+} titration of subdomain 1 monitored by 1D ^1H NMR. Ca^{2+}-induced, gradual chemical shift changes were observed at resonances in the main chain amide proton region, such as 7.76 (a) and 7.03 ppm (b). The Ca^{2+} concentrations from bottom to top were 0, 0.3, 0.7, 1.1, 1.5, 1.9, 2.8, 4.7, and 6.7 mM. (c) Chemical shift change plotted as a function of total Ca^{2+} concentration.

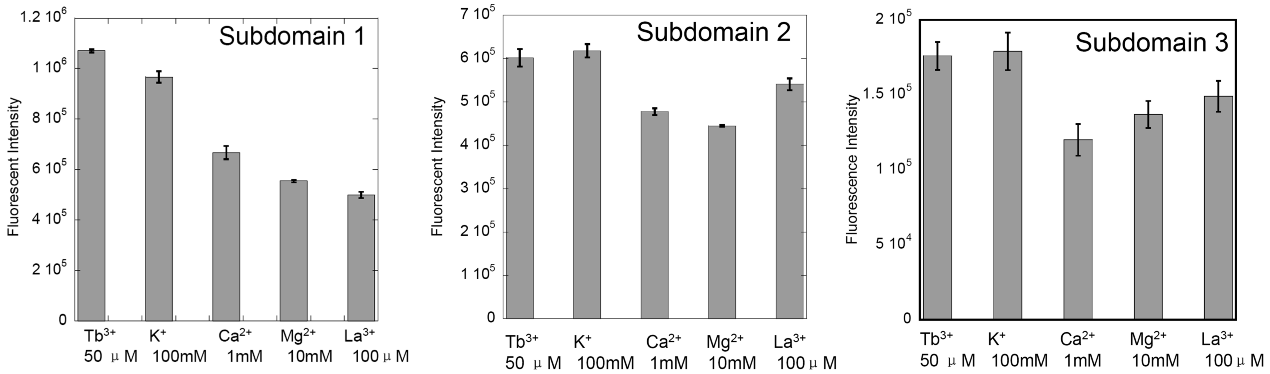

FIGURE 6: Metal competition assay for subdomains on the basis of Tb^{3+}-LRET. Protein samples (2 μM) were preincubated with 50 μM Tb^{3+}; 100 mM KCl, 1 mM $CaCl_2$, 10 mM $MgCl_2$, or 0.1 mM La^{3+} was subsequently added to individual Tb^{3+}-protein solutions. All the buffers consisted of 20 mM PIPES, 135 mM NaCl, and 10 mM KCl (pH 6.8).

and significantly weaker binding affinities for both the first ($K_d = 2.2 \pm 0.5$ μM) and second ($K_d = 21.5 \pm 2.7$ μM) steps. The binding curves were right-shifted after the substitution of charged ligand residues in either site of subdomain 3 with Ile (Figure 4c).

A notably biphasic binding process, similar to that depicted by the Tb^{3+} binding curve, was also observed for Ca^{2+} titration by monitoring ANS fluorescence. The dissociation constants obtained were 0.7 ± 0.1 mM for the first component and 6.4 ± 0.8 mM with a Hill coefficient of 3 for the second component (Figure 4b). Consistently, two distinct binding components were observed in one-dimensional (1D) ^1H NMR for subdomain 1. As seen in Figure 5, resonances in the main chain amide proton region, such as peaks at 7.76 ppm (Figure 5a) and 7.03 ppm (Figure 5b), exhibited gradual changes in chemical shift, whereas resonances corresponding to protons from aromatic side chain and methyl groups experienced changes in sudden peak shape and the appearance of more dispersed peaks when the Ca^{2+} concentration reached ~2 mM (Figure S3 of the Supporting Information). An apparent dissociation constant of 1.6 ± 0.1 mM and a Hill coefficient of 2.3 ± 0.2 were obtained by fitting chemical shift changes as a function of total Ca^{2+} concentration with a nonlinear Hill equation.

Metal Selectivity. In addition to Ca^{2+}, other metal ions, including Mg^{2+} and Ba^{2+}, are reported to function as agonists for the CaSR as revealed by functional assays (*36*). By utilizing the Tb^{3+}-LRET assay, we screened an array of monovalent (K^+), divalent (Ca^{2+} and Mg^{2+}), and trivalent (La^{3+}) metal ions for their effectiveness in competing for the protein-bound Tb^{3+}. As shown in Figure 6, for all the subdomains, the addition of a 2-fold excess of La^{3+}, a 20-fold excess of Ca^{2+}, and a 200-fold excess of Mg^{2+} to the Tb^{3+}-bound proteins is capable of competing for Tb^{3+} from the binding pockets and leads to a 15−50% decrease in the magnitude of the LRET signal. By comparison, the addition of a 200-fold excess of K^+ fails to dislodge Tb^{3+} from the binding sites.

Metal Binding Free Energies and Intradomain Cooperativity. The above-mentioned Hill coefficient is widely used to estimate intradomain cooperativity; however, this term reflects only the macroscopic properties of multiple metal binding processes and is not directly related to the true intradomain cooperative energy changes (*37*). A more accurate and quantitative way to analyze the intradomain cooperativity could be achieved by comparing the lower limit of intradomain cooperative energy (ΔG_C). We first tried using the two- or three-site Adair function to fit the whole biphasic Tb^{3+} binding curve (Figure 4a) and Ca^{2+} binding curve (Figure 4b). Surprisingly, all of our attempts at fitting either yielded a 1:1 binding mode (which is clearly not the case on the basis of visual inspection of the data) or were unsuccessful. However, by assuming that the free Ca^{2+} concentration is close to the total Ca^{2+} concentration, which can be justified because of the low affinity of the binding sites for Ca^{2+} and the use of protein concentrations 10−1000-fold lower than those of total and free Ca^{2+}, the second transition of both Tb^{3+} and ANS curves, and the cooperative curve obtained from NMR studies (Figure 5c), can be fitted with a two-site model-independent Adair function. We then analyzed all the titration data using the Adair function and calculated the changes in the total metal binding free energies (ΔG_2) and the lower limit of cooperative binding energy (ΔG_c) (Table 3). For Ca^{2+} binding to subdomain 1 (from

Table 3: Free Energies of Metal Binding to Subdomains of CaSR[a]

sample	metal	Gibbs free energy (kJ/mol) ΔG_1[b]	ΔG_2[b]	ΔG_c[c]	$\Delta\Delta G_2$[b]	$\Delta\Delta G_c$[c]
subdomain 1	Tb^{3+}	−12.0 ± 0.1	−24.5 ± 0.1	−3.9 ± 0.2	na	na
	Ca^{2+}[d]	−5.4 ± 0.1	−11.2 ± 0.2	−3.8 ± 0.3	na	na
	Ca^{2+}[e]	−5.0 ± 0.2	−10.9 ± 0.1	−4.4 ± 0.3	na	na
subdomain 1, mutation 1	Tb^{3+}	−12.1 ± 0.1	−23.3 ± 0.1	−2.4 ± 0.1	1.2 ± 0.2	1.5 ± 0.3
subdomain 1, mutation 2	Tb^{3+}	−11.4 ± 0.1	−22.4 ± 0.1	−3.0 ± 0.2	2.1 ± 0.2	0.9 ± 0.3
subdomain 2	Tb^{3+}	−11.6 ± 0.1	−22.6 ± 0.1	−2.9 ± 0.1	1.9 ± 0.2	1.0 ± 0.3
subdomain 3	Tb^{3+}	−10.1 ± 0.1	−20.1 ± 0.1	−3.3 ± 0.2	na	na
subdomain 3, mutation 4	Tb^{3+}	−10.2 ± 0.1	−19.4 ± 0.1	−2.4 ± 0.1	0.7 ± 0.2	0.9 ± 0.3
subdomain 3, mutation 5	Tb^{3+}	−9.9 ± 0.1	−19.1 ± 0.1	−2.7 ± 0.2	1.0 ± 0.2	0.6 ± 0.3

[a] Subdomain 1 and its mutant, as well as subdomain 2, exhibited biphasic metal binding. Only the second cooperative transition could be analyzed with the Adair function. Subdomain 1, mutation 3 was not included since it lacks the second transition. [b] ΔG_1 and ΔG_2 were obtained by fitting the titration data at 25 °C with eq 4. ΔG_1 reflects the sum of the free energy of the first ligand binding to each subdomain. Each domain is assumed to contain two Ca^{2+}-binding sites. ΔG_2 stands for the total free energy for the binding of two Ca^{2+} ions to the subdomain and accounts for any cooperativity between the two sites in each subdomain. $\Delta\Delta G_2 = \Delta G_{2,Tb}(\text{mutant}) - \Delta G_{2,Tb}(\text{WT})$. [c] By assuming that both sites in each subdomain have equal intrinsic Ca^{2+} binding affinities, the lower limit of free energy due to cooperative Ca^{2+} binding (ΔG_c) was calculated according to eq 5. $\Delta\Delta G_c = \Delta G_{c,Tb}(\text{mutant}) - \Delta G_{c,Tb}(\text{WT})$. [d] Data from Ca^{2+} titration monitored by changes in ANS fluorescence. [e] Ca^{2+} titration data from NMR experiments.

ANS fluorescence or NMR studies), the changes in total binding free energy ΔG_2 were found to be –10.9 to −11.2 kJ/mol. The intradomain cooperativity estimated by ΔG_c was between −3.8 and −4.4 kJ/mol, which is very close to the value obtained from Tb^{3+} binding data (−3.9 kJ/mol). After mutation of the predicted metal binding site 1 or 2 in subdomain 1, the changes in total binding free energy ΔG_2 were decreased by 1.2 or 2.1 kJ/mol, respectively. Compared to subdomain 1, subdomain 2, a truncated version of subdomain 1 that lacks the hinge region and part of predicted site 1, had a less favorable ΔG_2 with a $\Delta\Delta G_2$ of 1.9 kJ/mol. For subdomain 3, mutagenesis within site 4 or 5 also resulted in a less favorable ΔG_2, with a $\Delta\Delta G_2$ of 0.7 or 1.0 kJ/mol, respectively. All these results are consistent with the changes in macroscopic dissociation constants obtained by using the nonlinear Hill equation [K_{d2} (Table 2)]. More importantly, the apparent cooperativity reflected by ΔG_c was altered after mutation of key metal-binding residues within the predicted sites. In subdomain 1, the intradomain cooperativity was changed unfavorably by 1.5 kJ/mol in mutation 1 and 0.9 kJ/mol in mutation 2. Compared to subdomain 1, subdomain 2 also exhibited a lower intradomain cooperativity ($\Delta\Delta G_c$ = 1.0 kJ/mol). A similar scenario was observed in subdomain 3. A drop in the intradomain cooperativity by 0.7 or 1.0 kJ/mol was observed in mutation 4 or 5, respectively, of subdomain 3.

Mutations of Putative Ca^{2+}-Binding Ligand Residues Alter the Intracellular Ca^{2+} Response of the CaSR. To investigate the role of the proposed Ca^{2+}-binding sites in the biological functions of the CaSR, we introduced several mutations into the full-length intact CaSR (E297I in site 1 located at the crevice, D215I in site 2, and E228/229I in site 3). These mutants were overexpressed in HEK293 cells, which contain no endogenous CaSR (*3*). The effects of the mutations in the CaSR on intracellular Ca^{2+} signaling are summarized in Table 4 and Figure 7. Compared to wild-type CaSR, the mutant receptor containing the E297I mutation in site 1 exhibited significantly impaired sensitivity to $[Ca^{2+}]_o$ with an increase in EC_{50} from 2.8 ± 0.3 to 10.0 ± 0.2 mM and a decrease in the Hill coefficient from 2.9 ± 0.2 to 1.5 ± 0.2. In addition, the EC_{50} for the D215I mutant in site 2 increased to 6.3 ± 0.2 mM, while the maximal response in the E228I/E229I mutant in site 3 decreased to 64 ± 3%.

Table 4: Summary of the Intracellular Ca^{2+} Response in CaSR and Its Mutants

	EC_{50} (mM)	maximal response (%)	Hill coefficient
WT	2.8 ± 0.3	100	2.9 ± 0.2
E297I at site 1	10.0 ± 0.2[a]	89 ± 5	1.5 ± 0.2[a]
D215I at site 2	6.3 ± 0.2[a]	90 ± 2	2.5 ± 0.3
E228/229I at site 3	3.2 ± 0.3	64 ± 3[a]	2.6 ± 0.3

[a] $P < 0.01$.

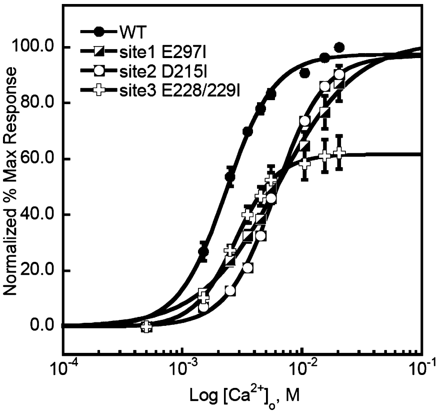

FIGURE 7: Intracellular Ca^{2+} response of HEK293 cells transiently overexpressing WT CaSR and its various mutants using Fura-2AM during stepwise increases in the extracellular Ca^{2+} concentration from 0.5 to 20.5 mM.

DISCUSSION

Correlation of Predicted Metal-Binding Sites with Disease-Associated Mutations. Responding to a narrow range of $[Ca^{2+}]_o$ values, the CaSR is able to trigger multiple intracellular signaling pathways, including cooperative changes in $[Ca^{2+}]_i$. The CaSR has been linked to a number of human diseases, such as FHH, NSHPT, and ADH (*7, 10*). Among these, FHH and NSHPT are characterized by a reduced sensitivity of the CaSR to $[Ca^{2+}]_o$, whereas the CaSRs of patients with ADH are oversensitive to changes in $[Ca^{2+}]_o$.

We have predicted five potential Ca^{2+}-binding sites within the CaSR's ECD based on homology modeling and analysis of its geometric properties and charge distributions. Figure 1 shows the model structure of putative Ca^{2+}-binding sites 1−3 and surrounding disease-associated mutations. In site 1, Y218S and E297K, with mutations on the ligand residues, and L174R, R185Q, and P221S, with mutations close to the ligand residues, inactivate the CaSR, while P221L activates the protein. Similarly, related to site 2, E250K is an inactivating mutation and Q245R is an activating mutation. Related to site 3, R220W and R220Q are inactivating mutations and E228Q is an activating mutation. Among these mutations, E297K, L174R, R185Q, Q245R, R220W, and R220Q might disturb the charge balance in the Ca^{2+}-binding pocket, resulting in a reduced Ca^{2+} binding affinity of the CaSR and thus an impaired Ca^{2+} sensitivity of the CaSR with a right-shifted intracellular Ca^{2+} response curve. The Y218S mutation is also expected to decrease the binding affinity of the CaSR for Ca^{2+} due to the much shorter side chain of Ser compared to that of Tyr. The mutations on P221 have opposite effects (*10*), possibly due to their different effects on the α-helical structures. Leu favors the formation of α-helix, while Ser is an unfavored residue for α-helix formation. The activating mutation, E228Q, could reduce the net negative charge of site 3 and reduce the degree of repulsion between those ligands, resulting in increased binding affinity for Ca^{2+}. The presence of disease-associated mutations within the proposed Ca^{2+}-binding ligands in all these predicted sites (Table 2) suggests a link between these diseases and the impaired Ca^{2+} binding capabilities of the respective mutant receptors.

Although no disease-associated mutations are present on the proposed ligand residues in sites 4 and 5, our previous functional data suggest that the mutations of the ligands in predicted site 5 lead to opposite effects on the $[Ca^{2+}]_i$ change in response to $[Ca^{2+}]_o$ (*19*). The double mutant E378I/E379I results in a left-shifted concentration−response curve to $[Ca^{2+}]_o$, whereas the double mutant E398I/E399I produces a right-shifted concentration−response curve to $[Ca^{2+}]_o$. The effects of other disease-associated mutations around the Ca^{2+}-binding sites on the Ca^{2+} binding properties will be a subject of further investigation in our laboratory.

Multiple Cooperative Metal Binding Processes. Functional studies as well as our metal binding studies demonstrate that CaSR has multiple Ca^{2+}-binding sites (*27*). We have previously investigated the site-specific metal binding properties of two continuous predicted sites (sites 3 and 5 in this study) by grafting them individually into the host protein, CD2 (*19*). Site-directed mutations on engineered proteins and the full-length CaSR support the idea that the predicted Ca^{2+}-binding residues are important in Ca^{2+} binding capability and in regulating CaSR functions. Interestingly, these probed site-specific Ca^{2+} binding affinities (4−20 mM) are weaker than the EC_{50} (2.7−3.1 mM) of the CaSR for Ca^{2+} (*19*), possibly due to the fact that the additional structural constraints imposed on the domain structures when they are in the intact ECD have additional effects not revealed in the structures of the isolated subdomains. In addition, some of the mutations within the predicted sites exhibit opposite effects on the protein's sensitivity to its native ligand. These observations indicate that binding of Ca^{2+} at different locations has diverse influences on the binding of subsequent Ca^{2+} ions and that the interaction of coupled metal-binding sites and cooperativity are likely to contribute to the overall capacity of the intact CaSR to respond to $[Ca^{2+}]_o$.

Dissection of metal-binding sites utilizing subdomains has been successfully applied to EF-hand Ca^{2+}-binding proteins, such as calmodulin and calbindin D_{28K} (*38, 39*). We have constructed three subdomains of the CaSR, and each subdomain contains two or three predicted Ca^{2+}-binding sites. The purified subdomains are well-folded as suggested by the CD, fluorescence, and NMR spectra. These well-folded domains allow us to visualize multiple metal binding processes within each subdomain and metal-dependent conformational changes within the subdomains.

Tb^{3+} and Ca^{2+} titrations clearly show that at least two distinct metal binding processes occur in subdomain 1. The fluorescence intensity and binding affinity are significantly reduced when any one of the three predicted sites is removed, indicating that the predicted Ca^{2+}-binding sites function in concert, and each site is crucial for maintaining the observed binding process. In particular, studies using site-directed mutagenesis suggest that predicted sites 1 and 3 are mainly responsible for the first and second components of the titration curve, respectively (Figure 4 and Table 2). The second transition is cooperative with an apparent intradomain cooperativity of −3.8 to −4.4 kJ/mol. Furthermore, the impaired Ca^{2+} binding ability coincides with abnormal $[Ca^{2+}]_i$ responses mediated by the CaSR in HEK cells. In particular, the E297I mutation in the full-length CaSR results in a striking right shift of the Ca^{2+} concentration−response curve. Concomitantly, the Hill coefficient was reduced from 2.9 ± 0.2 to 1.5 ± 0.2, which is in agreement with the abolition of the first binding process in subdomain 1 (Table 2 and Figure 4). Thus, it seems that site 1 has a higher binding affinity than site 2 and plays the major role in sensing low levels of plasma Ca^{2+}; in addition, the binding of Ca^{2+} to site 1, situated in the hinge region of the CaSR, lowers the energy barrier and enables further cooperative binding of Ca^{2+} ions to the other sites. This view is further corroborated by the fact that mutating key metal-binding residues in site 1 leads to a significant decrease in the changes in free energy for metal binding to subdomain 1 ($\Delta\Delta G_2$ = 1.2 kJ/mol) as well as a drop in the intradomain cooperativity of 1.5 kJ/mol. Our site-directed mutagenesis studies also suggest that predicted Ca^{2+}-binding site 3 in subdomain 1 plays unique roles in the Ca^{2+} binding and sensing events. The charged ligand mutations in this site abolished the second component of metal binding in subdomain 1 (Figure 4). Correspondingly, the maximal response of the mutant containing the E228I and E229I mutations in the full-length CaSR was significantly decreased, suggesting that site 3 is indeed crucial for transducing $[Ca^{2+}]_o$ to intracellular Ca^{2+} signals.

In subdomain 3, we also observed a cooperative binding curve, suggesting the existence of more than one binding site in the protein. Fitting the binding curve with a two-site Adair function resolves a lower limit of change in intradomain cooperativity, with ΔG_c of −3.3 kJ/mol. Similar to the scenario observed in subdomain 1, mutations on either of the two predicted sites (sites 4 and 5) result in significant decreases in ΔG_2 of 0.7−1.0 kJ/mol and lower the intradomain cooperativity by 0.6−0.9 kJ/mol. The metal selectivity screening experiments indicate that the CaSR has a wide spectrum of metal agonists, including at least Mg^{2+}, Ca^{2+}, and its trivalent analogues Tb^{3+} and La^{3+}, which is consistent with previous reports (*36*). This observed cooperativity could be the result of direct site-to-site interactions or Ca^{2+}-induced conformational change. If Ca^{2+} effectively cross-linked and neutralized negative charges in two different parts of the

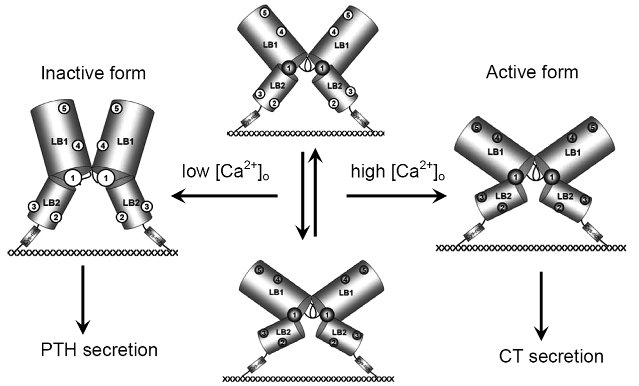

FIGURE 8: "Two-state" working model of CaSR. The active and inactive forms are in equilibrium, and the state of the receptor's activity varies in response to the association or dissociation of Ca^{2+} ions in the predicted Ca^{2+}-binding sites. High-affinity site 1 (with a K_d of ∼0.5−1 mM) is capable of sensing the normal range of [Ca^{2+}]$_o$ values. Both forms are in dynamic equilibrium in the normal physiological range of [Ca^{2+}]$_o$. Under low-[Ca^{2+}]$_o$ conditions, the Ca^{2+}-binding sites are largely devoid of ions, and the CaSR ECD exists as an inactive open form that favors PTH secretion. PTH is responsible for elevating [Ca^{2+}]$_o$. Under high-extracellular Ca^{2+} conditions, the binding of Ca^{2+} to all sites leads to conformational changes that favor activation of the receptor, which produces several homeostatic responses designed to normalize [Ca^{2+}]$_o$. These include inhibition of PTH secretion, stimulation of calcitonin (CT) secretion, a hormone that reduces [Ca^{2+}]$_o$, and enhancement of renal Ca^{2+} excretion. Thus, deviation from the state of homeostasis can be restored by the sensing of [Ca^{2+}]$_o$ by these putative Ca^{2+}-binding sites and the resultant reversible conformational changes. The filled circles indicate the loading of the sites with Ca^{2+}, while the empty circles indicate the absence of Ca^{2+}.

molecule, which then caused the lobes to close, then loss of one of those negative charges could reduce the level of repulsion between the negative charges that was present in the absence of Ca^{2+} and favor activation of the receptor at lower extracellular Ca^{2+} concentrations.

Ca^{2+}-Induced Conformational Changes. Ca^{2+}-induced conformational changes were observed in both fluorescence and NMR studies. The ANS binding assay further suggests that Ca^{2+} binding results in more exposure of hydrophobic regions. However, the removal of any one of the three predicted sites eliminates such significant Ca^{2+}-induced conformational changes. Suggested by the glutamate binding that occurs in mGluR1, the hinge that connects the two lobes directly responds to the stimulus-inducing receptor activation in the GPCR family C proteins. The predicted Ca^{2+}-binding site in the crevice is likely to play an important role in modulating the function of the CaSR by Ca^{2+}-induced conformational change (*19*).

On the basis of all these results, we postulate a working model for the CaSR with emphasis on the roles of the predicted Ca^{2+}-binding sites (Figure 8). Under normal physiological conditions with a [Ca^{2+}]$_o$ of 1.1−1.3 mM, the active and inactive forms of the CaSR are in dynamic equilibrium with each other. The "high-affinity" site (site 1 with a K_d of ∼0.5−1 mM) is responsible for the sensing and maintenance of this balance. If [Ca^{2+}]$_o$ is lower than the physiological level, the balance would shift to the inactive form of the CaSR and Ca^{2+} might dissociate from site 1, which would change the conformation of the CaSR. Such conformational changes are further relayed to the cytoplasm, leading to a signaling cascade favoring the secretion of PTH, which, in turn, elevates the extracellular level of Ca^{2+}. On the other hand, under abnormally high [Ca^{2+}]$_o$ conditions, the Ca^{2+}-binding sites are loaded with Ca^{2+} ions, and the CaSR exists in a conformation that is persistently activated. Ca^{2+} binding to weak sites (most probably sites 4 and 5 with affinities in the low millimolar range) results in further conformational changes that activate signaling cascades in favor of inhibition of PTH secretion as well as stimulation of renal Ca^{2+} excretion and secretion of calcitonin (CT), a hormone known to reduce the extracellular Ca^{2+} concentration. In this way, deviations from homeostatic balance can be self-corrected via modulation of the activities of different signaling pathways in cell types involved in maintaining Ca^{2+} homeostasis (e.g., parathyroid, kidney, and C-cells).

This model is consistent with the disease-associated mutations. In loss-of-function diseases, such as FHH/NSHPT, which are characterized by hypercalcemia, the Ca^{2+} binding ability of the CaSR is weakened, which shifts the balance to the inactive form. This leads to an increase in the level of PTH secretion, resulting in hypercalcemia. On the other hand, in the gain-of-function disease, ADH, some of the activating mutations increase the affinities of the Ca^{2+}-binding site(s), thereby inhibiting PTH secretion and renal tubular Ca^{2+} reabsorption and stimulating calcitonin secretion, which leads to hypocalcemia and hypercalciuria.

Overall, our findings provide further insights into the molecular mechanisms of the family of class III G protein-coupled receptors that are regulated by extracellular Ca^{2+} signaling. Our study describes a methodology for dissecting factors in Ca^{2+} binding, thereby contributing to our understanding of the general mechanism of Ca^{2+}-modulated conformational change in the CaSR, which can be correlated with its biological function. In addition, this study explores an approach to visualizing and probing Ca^{2+}-binding sites at simplified and more readily approachable levels, overcoming the obstacles encountered in expression and purification of highly hydrophobic membrane proteins. Indeed, this strategy for prediction and evaluation of Ca^{2+}-binding sites in the CaSR will likely also be useful for probing the roles of Ca^{2+} in many other proteins for which structural information is lacking.

ACKNOWLEDGMENT

We thank Dr. Hai Deng, Xue Wang, and Dr. G. T. Chen for the prediction of Ca^{2+}-binding sites in CaSR using GG. We thank Dan Adams for help in preparation of the manuscript and Mei Bai, Aldebaran Hofer, Hing-Cheung Wong, and other members from Yang group for their helpful suggestions.

SUPPORTING INFORMATION AVAILABLE

Summary of the Stern−Volmer quenching constants of subdomains (Table S1), modeled structures of subdomains 2 and 3 and SDS−PAGE of purified subdomains (Figure S1), near-UV CD spectra of subdomain 1 in the absence or presence of Ca^{2+} (Figure S2a), overall solvent accessibility of the tryptophan residues within each subdomain using fluorescence quenching with acrylamide (Figure S2b), and methyl group region of the 1D ^{1}H NMR spectrum of subdomain 1 (Figure S3). This material is available free of charge via the Internet at http://pubs.acs.org.

REFERENCES

1. Gao, Z. G., and Jacobson, K. A. (2006) Keynote review: Allosterism in membrane receptors. *Drug Discovery Today 11*, 191–202.
2. Brown, E. M., Gamba, G., Riccardi, D., Lombardi, M., Butters, R., Kifor, O., Sun, A., Hediger, M. A., Lytton, J., and Hebert, S. C. (1993) Cloning and characterization of an extracellular Ca^{2+}-sensing receptor from bovine parathyroid. *Nature 366*, 575–580.
3. Bai, M., Trivedi, S., and Brown, E. M. (1998) Dimerization of the extracellular calcium-sensing receptor (CaR) on the cell surface of CaR-transfected HEK293 cells. *J. Biol. Chem. 273*, 23605–23610.
4. Brown, E. M., Chattopadhyay, N., Vassilev, P. M., and Hebert, S. C. (1998) The calcium-sensing receptor (CaR) permits Ca^{2+} to function as a versatile extracellular first messenger. *Recent Prog. Horm. Res. 53*, 257–280.
5. Shapiro, L., and Colman, D. R. (1998) Structural biology of cadherins in the nervous system. *Curr. Opin. Neurobiol. 8*, 593–599.
6. Bai, M. (2004) Structure-function relationship of the extracellular calcium-sensing receptor. *Cell Calcium 35*, 197–207.
7. Hu, J., Mora, S., Colussi, G., Proverbio, M. C., Jones, K. A., Bolzoni, L., De Ferrari, M. E., Civati, G., and Spiegel, A. M. (2002) Autosomal dominant hypocalcemia caused by a novel mutation in the loop 2 region of the human calcium receptor extracellular domain. *J. Bone Miner. Res. 17*, 1461–1469.
8. Hu, J., Reyes-Cruz, G., Chen, W., Jacobson, K. A., and Spiegel, A. M. (2002) Identification of acidic residues in the extracellular loops of the seven-transmembrane domain of the human Ca^{2+} receptor critical for response to Ca^{2+} and a positive allosteric modulator. *J. Biol. Chem. 277*, 46622–46631.
9. Pearce, S. H. (2002) Clinical disorders of extracellular calcium-sensing and the molecular biology of the calcium-sensing receptor. *Ann. Med. 34*, 201–206.
10. Thakker, R. V. (2004) Diseases associated with the extracellular calcium-sensing receptor. *Cell Calcium 35*, 275–282.
11. Bai, M., Trivedi, S., Kifor, O., Quinn, S. J., and Brown, E. M. (1999) Intermolecular interactions between dimeric calcium-sensing receptor monomers are important for its normal function. *Proc. Natl. Acad. Sci. U.S.A. 96*, 2834–2839.
12. Mun, H. C., Franks, A. H., Culverston, E., Krapcho, K., Nemeth, E. F., and Conigrave, A. D. (2004) The extracellular Ca^{2+}-sensing receptor's venus fly trap domain is required for L-amino acid sensing. *J. Biol. Chem. 279*, 51739–51744.
13. Babu, Y. S., Bugg, C. E., and Cook, W. J. (1988) Structure of calmodulin refined at 2.2 Å resolution. *J. Mol. Biol. 204*, 191–204.
14. Kawasaki, H., and Kretsinger, R. H. (1995) Calcium-binding proteins 1: EF-hands. *Protein Profile 2*, 297–490.
15. Pertz, O., Bozic, D., Koch, A. W., Fauser, C., Brancaccio, A., and Engel, J. (1999) A new crystal structure, Ca^{2+} dependence and mutational analysis reveal molecular details of E-cadherin homoassociation. *EMBO J. 18*, 1738–1747.
16. Kunishima, N., Shimada, Y., Tsuji, Y., Sato, T., Yamamoto, M., Kumasaka, T., Nakanishi, S., Jingami, H., and Morikawa, K. (2000) Structural basis of glutamate recognition by a dimeric metabotropic glutamate receptor. *Nature 407*, 971–977.
17. Deng, H., Chen, G., Yang, W., and Yang, J. J. (2006) Predicting calcium-binding sites in proteins: A graph theory and geometry approach. *Proteins 64*, 34–42.
18. Yang, W., Wilkins, A. L., Ye, Y., Liu, Z. R., Li, S. Y., Urbauer, J. L., Hellinga, H. W., Kearney, A., van der Merwe, P. A., and Yang, J. J. (2005) Design of a calcium-binding protein with desired structure in a cell adhesion molecule. *J. Am. Chem. Soc. 127*, 2085–2093.
19. Huang, Y., Zhou, Y., Yang, W., Butters, R., Lee, H. W., Li, S., Castiblanco, A., Brown, E. M., and Yang, J. J. (2007) Identification and dissection of Ca^{2+}-binding sites in the extracellular domain of Ca^{2+}-sensing receptor. *J. Biol. Chem. 282*, 19000–19010.
20. Higgins, D. G. (1994) CLUSTAL V: Multiple alignment of DNA and protein sequences. *Methods Mol. Biol. 25*, 307–318.
21. Kopp, J., and Schwede, T. (2004) The SWISS-MODEL Repository of annotated three-dimensional protein structure homology models. *Nucleic Acids Res. 32*, D230–D234.
22. Schwede, T., Kopp, J., Guex, N., and Peitsch, M. C. (2003) SWISS-MODEL: An automated protein homology-modeling server. *Nucleic Acids Res. 31*, 3381–3385.
23. Marti-Renom, M. A., Stuart, A. C., Fiser, A., Sanchez, R., Melo, F., and Sali, A. (2000) Comparative protein structure modeling of genes and genomes. *Annu. Rev. Biophys. Biomol. Struct. 29*, 291–325.
24. Tsuchiya, D., Kunishima, N., Kamiya, N., Jingami, H., and Morikawa, K. (2002) Structural views of the ligand-binding cores of a metabotropic glutamate receptor complexed with an antagonist and both glutamate and Gd^{3+}. *Proc. Natl. Acad. Sci. U.S.A. 99*, 2660–2665.
25. Honig, B., and Nicholls, A. (1995) Classical electrostatics in biology and chemistry. *Science 268*, 1144–1149.
26. (a) Bai, A., and Honing, B. (1991) A rapid finite difference algorithm, utilizing successive over-relaxation to solve the Poison-Boltzmann equation. *J. Comput. Chem. 12*, 435445.
27. Bai, M., Quinn, S., Trivedi, S., Kifor, O., Pearce, S. H., Pollak, M. R., Krapcho, K., Hebert, S. C., and Brown, E. M. (1996) Expression and characterization of inactivating and activating mutations in the human $Ca^{2+}{}_{o}$-sensing receptor. *J. Biol. Chem. 271*, 19537–19545.
28. Gill, S. C., and von Hippel, P. H. (1989) Calculation of protein extinction coefficients from amino acid sequence data. *Anal. Biochem. 182*, 319–326.
29. VanScyoc, W. S., Sorensen, B. R., Rusinova, E., Laws, W. R., Ross, J. B., and Shea, M. A. (2002) Calcium binding to calmodulin mutants monitored by domain-specific intrinsic phenylalanine and tyrosine fluorescence. *Biophys. J. 83*, 2767–2780.
30. Pedigo, S., and Shea, M. A. (1995) Quantitative endoproteinase GluC footprinting of cooperative Ca^{2+} binding to calmodulin: Proteolytic susceptibility of E31 and E87 indicates interdomain interactions. *Biochemistry 34*, 1179–1196.
31. Rost, B., Yachdav, G., and Liu, J. (2004) The PredictProtein server. *Nucleic Acids Res. 32*, W321–W326.
32. McGuffin, L. J., Bryson, K., and Jones, D. T. (2000) The PSIPRED protein structure prediction server. *Bioinformatics 16*, 404–405.
33. Hu, J., and Spiegel, A. M. (2003) Naturally occurring mutations of the extracellular Ca^{2+}-sensing receptor: Implications for its structure and function. *Trends Endocrinol. Metab. 14*, 282–288.
34. Fan, G. F., Ray, K., Zhao, X. M., Goldsmith, P. K., and Spiegel, A. M. (1998) Mutational analysis of the cysteines in the extracellular domain of the human Ca^{2+} receptor: Effects on cell surface expression, dimerization and signal transduction. *FEBS Lett. 436*, 353–356.
35. Silve, C., Petrel, C., Leroy, C., Bruel, H., Mallet, E., Rognan, D., and Ruat, M. (2005) Delineating a Ca^{2+} binding pocket within the venus flytrap module of the human calcium-sensing receptor. *J. Biol. Chem. 280*, 37917–37923.
36. Handlogten, M. E., Shiraishi, N., Awata, H., Huang, C., and Miller, R. T. (2000) Extracellular Ca^{2+}-sensing receptor is a promiscuous divalent cation sensor that responds to lead. *Am. J. Physiol. 279*, F1083–F1091.
37. Forsen, S., and Linse, S. (1995) Cooperativity: Over the Hill. *Trends Biochem. Sci. 20*, 495–497.
38. Ye, Y., Lee, H. W., Yang, W., Shealy, S., and Yang, J. J. (2005) Probing site-specific calmodulin calcium and lanthanide affinity by grafting. *J. Am. Chem. Soc. 127*, 3743–3750.
39. Berggard, T., Miron, S., Onnerfjord, P., Thulin, E., Akerfeldt, K. S., Enghild, J. J., Akke, M., and Linse, S. (2002) Calbindin D28k exhibits properties characteristic of a Ca^{2+} sensor. *J. Biol. Chem. 277*, 16662–16672.

BI8014604